

# Simulating global dynamic surface reflectances for imaging spectroscopy spaceborne missions - LPJ-PROSAIL

Benjamin Poulter<sup>1</sup>, Bryce Currey<sup>2</sup>, Leonardo Calle<sup>2</sup>, Jack Brookshire<sup>2</sup>, Petya Campbell<sup>3</sup>, Adam Chlus<sup>4</sup>, Kerry Cawse-Nicholson<sup>5</sup>, Karl Fred Huemmrich<sup>6</sup>, Charles E. Miller<sup>4</sup>, Kimberley Miner<sup>4</sup>, Zoe Amie Pierrat<sup>7</sup>, David Schimel<sup>4</sup>, Shawn Paul Serbin<sup>8</sup>, Alexey N Shiklomanov<sup>9</sup>, E. Natasha Stavros<sup>10</sup>, Philip A Townsend<sup>11</sup>, David Ray Thompson<sup>5</sup>, Zhen Zhang<sup>12</sup>, Cibebe Amaral<sup>13</sup>, Ann Raiho<sup>1</sup>, and Jochen Stutz<sup>14</sup>

<sup>1</sup>NASA

<sup>2</sup>Montana State University

<sup>3</sup>University of Maryland, Joint Center for Environmental Technology (UMBC-JCET)

<sup>4</sup>Jet Propulsion Laboratory

<sup>5</sup>Jet Propulsion Laboratory, California Institute of Technology

<sup>6</sup>University of Maryland, Baltimore County

<sup>7</sup>UCLA

<sup>8</sup>Brookhaven National Laboratory (DOE)

<sup>9</sup>NASA Goddard Space Flight Center

<sup>10</sup>University of Colorado Boulder

<sup>11</sup>University of Wisconsin–Madison

<sup>12</sup>University of Maryland

<sup>13</sup>CU Boulder

<sup>14</sup>University of California Los Angeles

November 22, 2022

## Abstract

Imaging spectroscopy is a remote-sensing technique that retrieves reflectances across visible to shortwave infrared wavelengths at high spectral resolution (<10 nm). Spectroscopic reflectance data provide novel information on the properties of the Earth's terrestrial and aquatic surfaces. Until recently, imaging spectroscopy missions were limited spatially and temporally using airborne instruments, such as the Next Generation Airborne Visible InfraRed Imaging Spectrometer (AVIRIS-NG), providing the main source of observations. Here, we present a land-surface modeling framework to help support end-to-end traceability of emerging imaging spectroscopy spaceborne missions. The LPJ-wsl dynamic global vegetation model is coupled with the canopy radiative transfer model, PROSAIL, to generate global, gridded, daily visible to shortwave infrared (VSWIR) spectra. LPJ-wsl variables are cross-walked to meet required PROSAIL parameters, which include leaf structure, Chlorophyll a+b, brown pigment, equivalent water thickness, and dry matter content. Simulated spectra are compared to a boreal forest site, a temperate forest, managed grassland, and a tropical forest site using reflectance data from canopy imagers mounted on towers and from air and spaceborne platforms. We find that canopy nitrogen and leaf-area index are the most uncertain variables in translating LPJ-wsl to PROSAIL parameters but at first order, LPJ-PROSAIL successfully simulates surface reflectance dynamics. Future work will optimize functional relationships required for improving PROSAIL parameters and include the development of the LPJ-model to represent improvements in leaf water content and canopy nitrogen. The LPJ-PROSAIL model can support missions such as NASA's Surface Biology and Geology (SBG) and higher-level modeled products.

## Hosted file

essoar.10511508.1.docx available at <https://authorea.com/users/361858/articles/599341-simulating-global-dynamic-surface-reflectances-for-imaging-spectroscopy-spaceborne-missions-lpj-prosail>

*For AGU Special Collection 'Earth in Living Color'*

Simulating global dynamic surface reflectances for imaging spectroscopy spaceborne missions - LPJ-PROSAIL

Authors

Benjamin Poulter<sup>1</sup>, Bryce Currey<sup>2</sup>, Leonardo Calle<sup>3</sup>, Alexey N. Shiklomanov<sup>1</sup>, Cibele H. Amaral<sup>4</sup>, Jack Brookshire<sup>2</sup>, Petya Campbell<sup>1</sup>, Adam Chlus<sup>6</sup>, Kerry Cawse-Nicholson<sup>6</sup>, Fred Huemmrich<sup>1</sup>, Charles E Miller<sup>6</sup>, Kimberley Miner<sup>6</sup>, Zoe Pierrat<sup>7</sup>, Ann M. Raiho<sup>1,9</sup>, David Schimel<sup>6</sup>, Shawn Serbin<sup>8</sup>, Natasha Stavros<sup>4</sup>, Jochen Stutz<sup>7</sup>, Phil Townsend<sup>5</sup>, David R. Thompson<sup>6</sup> and Zhen Zhang<sup>9</sup>

<sup>1</sup>NASA Goddard Space Flight Center, Biospheric Sciences Lab., Greenbelt, MD 20771

<sup>2</sup>Montana State University, Land Resources, Bozeman, MT

<sup>3</sup>Regrow Agriculture Inc., Durham, NH 03824

<sup>4</sup>Earth Lab, Cooperative Institute for Research in Environmental Sciences, University of Colorado, Boulder, Boulder, CO 80309

<sup>5</sup>University of Wisconsin, Madison, WI

<sup>6</sup>Jet Propulsion Laboratory, California Institute of Technology, Pasadena, CA

<sup>7</sup>University of California Los Angeles, Los Angeles, CA

<sup>8</sup>Brookhaven National Laboratory, Upton, NY

<sup>9</sup>University of Maryland, ESSIC, Greenbelt, MD

## **Keywords**

Imaging spectroscopy; dynamic global vegetation model; Surface Biology and Geology (SBG); radiative transfer model;

## **Abstract**

Imaging spectroscopy is a remote-sensing technique that retrieves reflectances across visible to shortwave infrared wavelengths at high spectral resolution (<10 nm). Spectroscopic reflectance data provide novel information on the properties of the Earth's terrestrial and aquatic surfaces. Until recently, imaging spectroscopy missions were dependent mainly on airborne instruments, such as the Next Generation Airborne Visible InfraRed Imaging Spectrometer (AVIRIS-NG), providing limited spatial and temporal observations. Currently, there is an emergence of spaceborne imaging spectroscopy missions, which require advances in end-to-end model support for traceability studies. The LPJ-wsl dynamic global vegetation model is coupled with the canopy radiative transfer model, PROSAIL, to generate global, gridded, daily visible to shortwave infrared (VSWIR) spectra (400-2500 nm). LPJ-wsl variables are cross-walked to meet required PROSAIL parameters, which include leaf structure, Chlorophyll a+b, brown pigment, equivalent water thickness, and dry matter content.

Simulated spectra are compared to a boreal forest site, a temperate forest, managed grassland, and a tropical forest site using reflectance data from canopy imagers mounted on towers and from air and spaceborne platforms. We find that canopy nitrogen and leaf-area index are the most uncertain variables in translating LPJ-wsl to PROSAIL parameters but at first order, LPJ-PROSAIL successfully simulates surface reflectance dynamics. Future work will optimize functional relationships required for improving PROSAIL parameters and include the development of the LPJ-model to represent improvements in leaf water content and canopy nitrogen. The LPJ-PROSAIL model can support missions such as NASA's Surface Biology and Geology (SBG) and higher-level modeled products.

## Introduction

The reflectance of vegetation (Shull 1929, Gates et al., 1965), and its scaling from leaf to canopy, reveals information on vegetation health, taxonomic and functional composition, and ecosystem processes. Early vegetation indices (Kriegler et al., 1969) linked light reflectance in the red and near-infrared to chlorophyll and leaf water content (Tucker 1979). Vegetation indices such as the Normalized Difference Vegetation Index (NDVI) have since been used to infer net primary production (NPP) and biomass accumulation (Tucker & Sellers 1986). These indices have advanced to more precisely control for the effects of atmospheric conditions, i.e., the Enhanced Vegetation Index, EVI (Huete et al., 2002), or the removal of non-photosynthetic pigments, i.e., the Near-Infrared Reflectance of Vegetation, NIRv (Badgley et al., 2019).

Beyond traditional two-band vegetation indices that rely on multispectral reflectance data are reflectance retrievals using imaging spectroscopy (Rast & Painter, 2019). Imaging spectroscopy, also known as hyperspectral remote sensing, can resolve spectral information in ~3-10 nm increments for the visible to shortwave infrared region (VSWIR; 400-2500 nm) and thus be integrated within a variety of modeling approaches to estimate leaf and canopy properties (Wold et al., 2001, Gamon et al., 2019). When quantified, the chemical and physical constituents of vegetation canopies, such as chlorophyll and carotenoid content, leaf dry matter, and leaf water content, can improve our understanding of terrestrial carbon, water, and energy budgets. For example, retrievals of vegetation canopy chemistry can provide insights into photosynthesis (Campbell et al., 2022), potentially reducing uncertainty in key components of the global carbon cycle, for example, where global gross primary production estimates range from 103-166 PgC yr<sup>-1</sup> (Norton et al., 2019).

The use of imaging spectroscopy has so far been limited mostly to airborne observations, which sample discrete spatial and temporal domains; for example, the AVIRIS-NG instrument has been used in specific campaigns over North America, Europe, and India. Spaceborne imaging spectroscopy has been carried out via pathfinder missions such as NASA's Hyperion mission (Folkman et al., 2001; Middleton et al., 2017), the Italian Space Agency's (ASI) Hyperspectral Precursor of the Application Mission (PRISMA) (Loizzo et al., 2018; Cogliati et

al., 2021), the Japanese Space Agency’s Hyperspectral Imaging Suite (HISUI), and the German Aerospace Center (DLR) Earth Sensing Imaging Spectrometer, DESIS (Krutz et al., 2019; Alonso et al., 2019). These missions also tend to have limited acquisition strategies, mission duration, or do not cover the full VSWIR range.

Over the next decade, an emergence in Earth observations using imaging spectroscopy will take place; in early 2022, DLR launched the Environmental Mapping and Analysis Program (ENMAP), and in the summer of 2022, NASA will launch Earth Surface Mineral Dust Source Investigation (EMIT, Connelly, et al., 2021). By the end of this decade, NASA will have launched the Surface Biology and Geology (SBG) mission (Stavros et al., 2022, Schimel & Poulter, 2022), and ESA will have launched the Copernicus Hyperspectral Imaging Mission for the Environment (CHIME) mission (Nieke & Rast, 2018), providing global VSWIR retrievals at 10-nm spectral resolution, with high signal-to-noise, 30-m spatial resolution, and with potentially less than eight days revisit when the SBG and CHIME constellation are taken together.

End-to-end (E2E) simulators will play an important role in supporting the traceability of mission requirements and in providing pre-launch characterization of expected science and applications products (Verrelst et al., 2021). E2E simulators quantify instrument, retrieval, and algorithmic uncertainties and the propagation of these uncertainties under various workflows. For example, the Hypertrace workflow was developed for SBG to assess science value trades and algorithm performance (Cawse-Nicholson et al., in review, Raiho et al., in review). Three dimensional radiative transfer models (RTMs), such as the Digital Imaging and Remote Sensing Image Generation (DIRSIG, Schott et al., 1999, Lentilucci and Brown, 203) and Discrete Anisotropic Radiative Transfer (DART, Gastellu-Etchegorry et al., 2015), can also inform E2E as they provide a controlled simulation environment whereby surface leaving reflectances are represented via detailed 3-dimensional representation of objects and the scattering, absorption and transmission of light (Goodenough and Brown, 2012). These approaches use ray-tracing methods that are computationally intensive and thus limited to small areas and single points in time.

Alternatively, more computationally efficient two-stream radiative transfer approximations make generalized assumptions about leaf structure (i.e., gas-like behavior) that can be used to simulate reflectance (Yuan et al., 2017). Combined with process-based models, such as land-surface models and ocean biogeochemistry models, 2-stream RTMs can also inform E2E as the basis of Observing System Simulation Experiments (OSSE, Gelaro et al., 2009). For example, ocean biogeochemical models coupled with RTMs can simulate water-leaving radiances supporting NASA’s Plankton, Aerosols, Cloud and Ocean Ecosystem (PACE) mission instrument design and algorithm performance (Gregg et al., 2017; Fan et al., 2021). For the land surface, the coupling of vegetation models and RTMs has been shown to produce canopy VSWIR spectra that are comparable to observations (Shiklomanov et al., 2020, Antonarakis et al., 2022) and

provide insights into plant traits and chemical composition.

Here we describe the development of LPJ-PROSAIL, where LPJ is a dynamic global vegetation model (DGVM) developed for global-scale studies of vegetation dynamics and biogeochemistry (Sitch et al., 2003), and PROSAIL is a canopy radiative transfer model (Jacquemoud et al., 2009) that combines leaf optical properties to simulate bidirectional reflectances. The integration of the two modeling approaches enables simulation of global scale, gridded time series of daily vegetation reflectances to be simulated. We evaluate the performance for four intensive sites and globally (Figure 1). This activity supports NASA’s SBG E2E tools and provides an opportunity to evaluate data volumes and formats, to assess instrument and algorithm performance, and to explore Level 4 and Level 5 mission products.

## Methods

### *LPJ dynamic global vegetation model*

The LPJ dynamic global vegetation model was developed in 2003 and couples dynamic representation of vegetation demography with a mechanistic representation of plant physiology and biogeochemistry at a daily time step (Sitch et al., 2003; Calle & Poulter, 2021). Photosynthesis is represented by the Farquhar biochemical model, determined as a co-limited process between maximum carboxylation capacity ( $V_{cmax}$ ), electron transport ( $J_{max}$ ), and sucrose utilization (Farquhar et al., 1980).  $V_{cmax}$  is estimated prognostically, as a function of photosynthetic active radiation (PAR), air temperature, and shortwave radiation, based on optimality theory to maximize photosynthesis when radiation is at its peak (Haxeltine & Prentice, 1996). The canopy is represented as a single big leaf (Fisher et al., 2018), with no distinction for sun or shade-lit leaves, and applies Beer’s Law to approximate vertical light profile to estimate the fraction of absorbed photosynthetic active radiation used in photosynthesis. A ‘two-bucket’ soil hydrology model is coupled to stomatal conductance, via water demand and supply, to limit  $CO_2$  diffusion from the atmosphere to leaf under drought conditions (when atmospheric demand is greater than soil water supply).

Relevant for the coupling of LPJ with PROSAIL are the variables that inform the five leaf optical properties required by the sub-model PROSPECT-5b (Feret et al., 2008). These properties are the leaf structure parameter ( $n_{layers}$ ), Chlorophyll a + b content ( $Cab$ ), equivalent water thickness (EWT), dry matter content ( $Cm$ ), and brown pigment ( $Cbrown$ ). Within LPJ, vegetation is represented through ten plant functional types (PFTs), that establish according to bioclimatic constraints and compete with one another for space, light, and water. The PFTs are characterized by leaf, fine root, sapwood and heartwood biomass pools for woody functional types and leaf and fine root pools for grasses. Leaf area index (LAI) is estimated by integrating specific leaf area with leaf biomass and scaled by a phenology ‘ramp’ factor determined by growing-degree day requirements (Sitch et al., 2003).

### *PROSAIL: The PROSPECT 5-b and 4SAIL model*

PROSAIL combines the PROSPECT 5-b generalized plate directional-hemispherical model (Feret et al., 2008) and the 4SAIL (Scattering by Arbitrary Inclined Leaves) canopy reflectance model (Verhoef et al., 2007). PROSAIL simulates canopy reflectance from 400-2500 nm (at 1 nm resolution) by passing leaf optical properties (reflectance and transmittance) from PROSPECT through to 4SAIL, a four-stream radiative transfer approximation, which incorporates sun-angle geometry and filtering through a canopy. Using 14 input variables (see sections below for parameterization), five from PROSPECT-5b and eight from 4SAIL (Table 1), PROSAIL therefore links spectral variation in canopy reflectance to leaf biochemical properties, canopy architecture, and soil/vegetation interactions (Figure 2a).

PROSAIL estimates four reflectance factors for directional or hemispherically-integrated incident (incoming) and exitant (outgoing) light as a function of latitude, time of year, and time of day that are integrated across the canopy to provide four reflectances. The four reflectances are the pairwise combination of incident and exitant direct (i.e., directional, beam, collimated, or angle-dependent) vs. diffuse (i.e., hemispherical, hemispherically-integrated, uncollimated, or angle-independent) radiation. Explicitly, the four reflectance outputs from PROSAIL are bi-directional reflectance (BRD (coded as RSOT); i.e., direct in, direct out); directional hemispherical reflectance (DHR (RSDT); i.e., direct in, diffuse out), hemispherical-directional reflectance (HRD (RDOT); i.e., diffuse in, direct out), and bi-hemispherical reflectance (BHRF (RDDT); i.e., diffuse in, diffuse out).

Some of the streams are insensitive to certain parameters, e.g., hot-spot has no effect on the hemispherical reflectance outputs (Schaeppman-Strub et al., 2006). Of importance, PROSAIL does not estimate radiance, only reflectance, thus is independent of the amount or quality of incident light. PROSAIL does take as input the solar zenith and azimuth angles for incident light, but those only affect the incident directional reflectance outputs. Solar zenith and azimuth angles affect the reflectance factors for incident direct (beam) radiation (i.e., the directional-hemispherical and bi-directional reflectance factors).

For the purpose of comparison, BHR is the closest representation of intrinsic surface properties, but BHR is insensitive to observer zenith angle by definition. As such, to compare with airborne and satellite instrumentation, we focus on bi-directional reflectance (BDR; RSOT) and hemispherical-directional reflectance (HDR; RSDT) as this is what most closely represents what airborne and satellite instruments actually measure to create a fifth reflectance output from LPJ-PROSAIL called total top-of-canopy outgoing directional radiation ( $TOC_{ref}$ ).  $TOC_{ref}$  is scaled by PAR, is in the sensor direction, and is estimated as the ratio of BDR and HDR as follows:

$$TOC_{ref} = \frac{(RSOT \times PAR_{dif} + RSDT \times PAR_{dir})}{(PAR_{dir} + PAR_{dif})} \text{ Equation 1}$$

$$PAR_{dir} = (1-SKYL)Es \text{ Equation 2}$$

PARdif = (SKYL)Ed Equation 3

SKYL=0.847-1.61 x sin((90-tts) x ( $\frac{\text{Pi}}{180}$ ))+1.04 x sin((90-tts) x ( $\frac{\text{Pi}}{180}$ )) x sin((90-tts) x ( $\frac{\text{Pi}}{180}$ )) Eq. 4

Where Es and Ed are wavelength-specific direct and diffuse energy from the sun, respectively, as specified by Feret et al., (2008) and *tts* is the solar zenith angle as defined by latitude, date and time of day. This approach results in a ratio of total direct radiation to diffuse radiation of roughly 0.8 assuming cloud free conditions.

#### *Integrating LPJ and PROSAIL*

For integration with LPJ-wsl 2.0, the PROSAIL model code was translated from Fortran 90 to C (the codebase of LPJwsl) based on <http://teledetection.ipgp.jussieu.fr/prosail/>. LPJ calls on PROSAIL sub-routines daily when vegetation is present (i.e., LAI => 0). When LAI is equal to 0, the reflectances are equal to a weighted average of (i) soil, (ii) branch (if present), or (iii) snow reflectances (if present; see next section). Five of the 14 PROSAIL inputs (Table 1) are dynamic and based on PFT-specific temporal variation. The eight 4SAIL parameters are derived from LAI and from latitude, day of year, and time of day. The spectral response functions are output for each grid cell at either daily or monthly timesteps. The user is provided a series of compiler flags that determine whether to run LPJ-PROSAIL (flag PROSAIL), the spectral resolution (LAMBDA\_BINWIDTH), the output frequency (DAILY or MONTHLY), start year for writing, and an experimental averaging of trait values to inform PROSPECT-5b rather than area-weighted averaging of PFT, soil and snow spectra.

#### *PROSPECT-5b: chlorophyll content (Cab)*

We derive chlorophyll a and b (*Cab*) from LPJ's prognostic PFT specific canopy Vcmax (mol CO<sub>2</sub> m<sup>-2</sup> s<sup>-1</sup>) based on empirical relationships between the quantities derived in Croft et al. (2017). For deciduous phenology PFTs, a 10-day running average of Vcmax is estimated to smooth day-to-day variability where PAR equal to zero causes Vcmax to drop to zero (Haxeltine & Prentice, 1996). For evergreen phenology PFTs, we assumed Vcmax was equal to the previous year's maximum value to avoid artifacts from the strong optimality assumption of Haxeltine and Prentice (1996), which drives Vcmax to zero at low temperature or low PAR values. We standardize Vcmax to 25°C (Vcmax25) using Equations 8.9 to 8.11 for C3 and C4 photosynthetic pathways from Oleson et al., (2013). For all PFTs, *Cab* is estimated by Croft et al. (2017) as:

$$Cab = \frac{(Vcmax25-3.72)}{1.3}$$
 Equation 5

#### *PROSPECT-5b: Equivalent water thickness (Cw)*

Cw is measured in units of cm, and the maximum value is around 0.01 cm (Jacquemond and Ustin, 2019). Cw is challenging to derive from land-surface models as field studies for calibration are sparse or involve scaling assumptions

that are not directly comparable to modeled variables. Stand-scale metrics of field measured  $C_w$  i.e., Roberts et al. (2004), show that  $C_w$  scales intrinsically with LAI, thus is a combination of canopy structure and leaf internal water, but PROSAIL requires leaf level  $C_w$ .

We instead approximate  $C_w$  from soil moisture in the uppermost soil layer of LPJ, using an exponential scaling factor ( $\alpha=5.5$ ), providing a  $\max C_w=0.01$  and  $\min C_w=0.0$  (see Figure 2b). The uncertainty of this approach is evaluated at first-order by changing the shape of the response function and future work will calibrate this relationship for each PFT using tower or airborne measurements.

$$C_w = (\max C_w - (\max C_w - \min C_w)) * e^{-\alpha * \text{soilmoisture}} \text{ Equation 6}$$

*PROSPECT-5b: Carotenoid (Car) and Brown Pigment (Cbrown)*

The total carotenoid content ( $Car$ ) is maintained at a constant  $8.0 \text{ ug cm}^{-2}$  as in Feret et al., (2008). Leaf brown pigment ( $C_{brown}$ ) is useful for discriminating between photosynthetic and non-photosynthetic (i.e., polyphenols, tannins, secondary metabolites, and defensive compounds in the leaves) light absorption within a leaf.  $C_{brown}$  is poorly defined in the literature, and its interpretation varies from, most commonly, brown pigment concentrations (such as phenols or tannins) to the color of senesced leaves (Danner et al., 2019). Therefore, we set  $C_{brown}$  to a constant value (0.01) to reduce dynamic uncertainty.

*PROSPECT 5-b: Leaf structure (n\_layer), Dry matter content (Cm)*

The leaf structure coefficient ( $n\_layer$ ) is the number of compact layers specifying the average number of air and cell wall interfaces within the mesophyll cells of the leaves. We vary  $n\_layer$  based on its relationship with specific leaf area ( $SLA$ ,  $\text{g cm}^{-2}$ ) and the proposed hyperbolic relationship from Jacquemond and Baret (1990) and Ceccato et al., (2001):

$$n\_layer = \frac{(0.9 \text{ SLA} + 0.025)}{(\text{SLA} - 0.01)} \text{ Equation 7}$$

Dry matter content,  $C_m$  ( $\text{g cm}^{-2}$ ), is estimated from LPJ PFT specific specific leaf area ( $SLA$ ):

$$C_m = \frac{1}{\overline{SLA}} \text{ Equation 8}$$

*4SAIL*

4SAIL requires eight parameters related to canopy structure and to solar and viewing geometry. LAI is PFT specific and varies daily, and is used directly as an input to 4SAIL. The leaf inclination distribution function (LIDF) consists of two components, average leaf slope (LIDFa) and the leaf distribution bimodality (LIDFb). We assume a spherical LIDF, with LIDFa equal to -0.35 and LIDFb equal to -0.15 (Campbell et al., 1990; Verhoef et al., 1998).

The hot spot parameter ( $S_L$ ), defined as the ratio of leaf width to canopy height, for our simulations, we assume to be no shadow (0.01), i.e., pure hot spot, to reflect no canopy obstructions. The 4SAIL soil reflectance factor ( $p_s$ ) is assumed

Lambertian (see Hapke et al., 1981, Verhoef and Bach 2007) and is a function of LPJ soil moisture (SM) in the upper layer:

$$p_s = \text{SM} \cdot \text{R1} + (1 - \text{SM}) \cdot \text{R2} \text{ Equation 9}$$

Where R1 and R2 are empirically-derived dry and wet soil reflectances, respectively (Feret et al., 2008).

Sun-observer viewing zenith angle (vza) is fixed to nadir, 0-degrees. Solar zenith angle (sza) and relative azimuth angle (raa) are estimated from day of year, latitude, and time of day (assuming a 10:30 am local time overpass).

#### *Reflectances for branches and snow*

PROSAIL does not include reflectances for woody components (branches), water, snow or ice but does incorporate soil reflectance into the reflectance estimates. When LAI is zero, PROSAIL assumes that the reflectance is composed entirely of the background/soil component. In the basic 4SAIL model (Verhoef et al., 2007) the background component is based on a soil reflectance spectrum provided by a modified version of the Hapke model that includes a soil moisture effect and accounts for a hotspot effect, e.g., Eq. 9. To expand the realism of our simulation and to avoid the assumption of background reflectance only coming from soils, we instead took representative spectra for branches from the ECOSTRESS spectral library (Meerdink et al., 2019) and snow from Stamnes et al., (1988) and mixed these with the spectra simulated from PROSAIL (see Supplementary Figure 2 for the branch, snow spectra). We do not include open water or ice spectra.

Representative snow spectra  $> 1500$  nm was smoothed using a loess smoother due to very high noise ( $k = 2$ ,  $\text{span} = 0.15$ ). The spectra for branches and snow are mixed with the PROSAIL spectra based on the following simple assumption that when  $\text{LAI} < 1$ , the PROSAIL spectra are mixed with branch or snow as follows:

if  $\text{LAI} < 1$  and snow depth (mm) == 0

$$\text{TOC}_{\text{rad}} = \text{lai} \cdot \text{canopy reflectance} + (1 - \text{lai}) \cdot \text{branch reflectance} \text{ Equation 10}$$

if  $\text{LAI} < 1$  and snow depth  $> 0$  (assumes branches are covered)

$$\text{TOC}_{\text{rad}} = \text{lai} \cdot \text{canopy reflectance} + (1 - \text{lai}) \cdot \text{snow reflectance} \text{ Equation 11}$$

if  $\text{LAI} == 0$  and snow depth == 0

$$\text{TOC}_{\text{rad}} = \text{soil reflectance} \text{ Equation 12}$$

if  $\text{LAI} == 0$  and snow depth  $> 0$  (assumes soil and branches are covered)

$$\text{TOC}_{\text{rad}} = \text{snow reflectance} \text{ Equation 13}$$

This approach assumes that snow does not accumulate on the vegetation canopy and only masks out the soil reflectance. In future, wood area index (WAI,

Kuusinen et al., 2021) will be estimated to more realistically determine the branch area and contribution to reflectance.

#### *Averaging spectra to the grid cell*

PROSAIL is applied to each PFT following the steps described previously to estimate parameters for PROSPECT-5b and 4SAIL, and the mixing of branch and snow, if present. The individual PFT spectra are then averaged together, weighting the average based on the fractional coverage of each PFT within a grid cell.

#### *Simulations: Site descriptions and global set up*

LPJ-PROSAIL was run globally at 0.5-degree spatial resolution using meteorological forcing from the Climatic Research Unit for years 1901-2020, v4.05 (Harris et al., 2020) and soil data from the Harmonized World Soils Database version 2.0. The land-use change module was not used in the simulations, and only the distribution and physiology simulated for natural PFTs. The year 2020 was the output for evaluating the spectra. Four sites were selected for evaluation (Figure 1 B-E), these include sites equipped with canopy spectrometers and data available from the DESIS and PRISMA imaging spectrometers. The four sites included tropical, temperate forest, temperate cropland, and boreal forest.

The “Southern Old Black Spruce” site (SOBS) in Saskatchewan was used as a representative boreal forest (latitude/longitude: (53.98°N, 105.12°W). The SOBS site is a mixed forest stand with a stand density of ~10% larch (*Larix laricina*) and ~90% black spruce (*Picea mariana*). Canopy reflectance spectra were collected using PhotoSpec using an Ocean Optics Flame Spectrometer (400-900 nm; Grossman et al., 2018, for full instrument description). PhotoSpec was installed atop the site’s 25-m scaffolding tower and collected data from September 2018-April 2021. PhotoSpec has a narrow field of view (0.7 degrees) and takes a representative canopy scan over 44 target locations every 30 minutes (Pierrat et al., 2021, 2022). 30-minute representative canopy averages were filtered for clear sky conditions and averaged monthly over the entire collection period between 10:00-14:00 to reflect an approximate satellite overpass time equivalent to PROSAIL configuration.

The temperate forest site is Blackhawk Island, WI, USA (43.65° N, 89.79° W), a 73-ha island in the Wisconsin River. The island is composed of a mix of broadleaf and coniferous species, including oak (*Quercus*), maple (*Acer*), and pine (*Pinus*) species. A HySpex imaging spectrometer was used to measure full range canopy reflectance (400-2400 nm) at 1-m spatial resolution over Blackhawk Island on eight dates during the 2018 growing season (May-October) (Chlus & Townsend, 2022).

The Beltsville site is managed by the USDA Agricultural Research Service in Beltsville, Maryland (39.030686°N, 76.84546°W). The local climate is temperate with hot and humid summers, long fall and typically mild winters, which

strongly vary in seasonal leaf area index, canopy chlorophyll, and biomass patterns. The site is a 22 ha rainfed maize production field, planted annually and maintained under optimal nitrogen treatment, monitored by an eddy covariance tower. During the 2017-2020 time period, the site was instrumented with an automated canopy spectrometer system Dual FLuorescence boX (FloX, JB Hyperspectral Devices UG, Dusseldorf, Germany; Julitta et al., 2017), collecting diurnal reflectance measurements throughout the seasons. The FLoX downwelling optics were mounted at the top of a portable platform at approximately 3 m height. The upwelling optics were positioned at nadir and maintained at 1.5 m above the canopy throughout the growing season, by lifting periodically the measurement arm as new leaves developed and the canopy grew taller, viewing a 25° field of view (Campbell et al., 2019; Campbell et al., 2022).

The tropical site is La Selva, Costa Rica, an evergreen tropical forest where a PhotoSpec imager is located on a 40-m tower providing continuous reflectance information from 400-1000 nm. The same measurement and data filtering and aggregation approach was used for this site that was developed for the SOBS site.

#### *Remote-sensing Observations*

Currently, two spaceborne imaging spectrometers are providing hyperspectral reflectance observations, DESIS and PRISMA. Data from HISUI aboard the International Space Station are currently unavailable, and tearly April 2022. We acquired the spectra for DESIS and PRISMA for three sites from [teledyne.tcloudhost.com](http://teledyne.tcloudhost.com) and [prisma.asi.it](http://prisma.asi.it) for the months June to August of 2020 and 2021. DESIS covers the spectral range 400-1000 nm (VNIR) with bandwidth of 3.5 nm and spectral sampling of 2.5 nm, totaling 235 channels. PRISMA covers the full VSWIR spectrum, i.e. 400-2500 nm, with bandwidth of 12 nm and spectral sampling of about 9.3 nm resulting in 240 bands. Both sensors collect data at 30-m spatial resolution. The used images were collected with clear-sky conditions over the target sites and rated as ‘acceptable’ during the quality assessment. We downloaded surface reflectance products processed to levels 2A (DESI) and 2D (PRISMA) and extracted the average spectra from 2x2 pixels (3,600 m<sup>2</sup>) polygons around the site’s central coordinates.

AVIRIS-NG data were used for the boreal (flight ID = ang20170817t180204) and temperate (flight ID = ang20190620t150429) forest site (Gao et al., 1993; Thompson et al., 2015). For the boreal site, atmospherically reflectance was available to download. However, the boreal forest site location was shaded by clouds in the available image, so we selected 25 evergreen spectra in the vicinity of the site and reported the average across the wavelengths. For the temperate forest site, radiance for the single site was downloaded and processed through atmospheric correction software, Imaging Spectrometer Optimal FITting (ISOFIT; Thompson et al., 2018), to obtain site-level reflectance.

#### *Analysis*

The analysis consists of qualitative and quantitative comparisons between the

simulated and observed spectra. The assumptions and uncertainty for Cw functional form are evaluated.

## Results and Discussion

### *Crosswalking of LPJ to PROSAIL*

We made various assumptions to provide the parameters required for PROSAIL listed in Table 1. For PROSPECT-5b, the parameters  $n\_layers$ ,  $Cab$ ,  $Cw$ , and  $Cm$  were estimated directly from LPJ variables, and for  $Car$  and  $Cbrown$ , we used constant values due to lack of information. The main sources of error identified were in LAI, where values over the grassland site were unreasonably high, and in  $Vcmax$ , where values in the temperate forest site were lower than observed. Assumptions in the functional forms used to approximate leaf water content were evaluated through sensitivity analysis. The mixing of spectra from snow, branch and soil assumed linear mixing with the potential to explore more complex weighting schemes in the future. From a theoretical perspective, LPJ represents canopy structure via a simplistic big-leaf approximation and Beer's Law to approximate light penetration within the canopy. In addition, scaling assumptions between LPJ and PROSAIL, i.e., simplification of canopy structure by LPJ, versus representation of lead and air space in PROSAIL, differ from one another and drive uncertainties.

### *Site level characteristics*

For the individual sites, Figures 3-7, LPJ-PROSAIL simulated full VSWIR spectral response functions, including their month-to-month temporal and spatial variability. The boreal site (Figure 3) showed seasonal reflectances that included a snow signal for winter months mixing with the canopy reflectances. The temperate forest site (Figure 4) showed higher seasonal variation in the spectra compared to the boreal site because of the greater abundance of deciduous PFTs. High reflectance in the red region was symptomatic of low  $Vcmax$  values simulated by LPJ ( $30-40 \text{ mol CO}_2 \text{ m}^{-2} \text{ s}^{-1}$ ) in comparison to measured values ranging from  $60-100 \text{ mol CO}_2 \text{ m}^{-2} \text{ s}^{-1}$ . The temperate managed grassland (Figure 5) had less seasonal variation, and changes in the spectra were mainly from seasonality in  $Vcmax$ . At the tropical site, low seasonal variation in the spectra was simulated due to a combination of little to no seasonality in LAI.

Compared to observations, Figure 7, LPJ-PROSAIL tended to have a positive bias in reflectance across the full VSWIR range. This is mainly due to the LPJ LAI being higher ( $\sim 10 \text{ m}^2 \text{ m}^{-2}$ ) than what is realistic. The spectral features were generally similar to the observations from the tower, but the space-based spectra differ significantly from both model and tower reflectance and from each other. This could be related to the remote instruments' calibration or atmospheric correction; for example, sharp spectral features at 940 nm and 1140 nm are likely artifacts from atmospheric water vapor absorption. Sun-sensor viewing geometries were held constant for PROSAIL, but compared to the tower observations the view angles and field of view introduce significant biases. Figure 8 uses Hoevermueller plots to illustrate how the full VSWIR spectra

evolve over a representative calendar year (2020). For each site, the reflectance features show the simultaneous effects of changes in biochemistry, vegetation structure, soil, snow, and branch mixing.

#### *Sensitivity in leaf water content*

Figure 9 shows the biases of the spectra for June (2020) in relation to how the functional form of  $C_w$  to soil moisture is parameterized. The non-linear (default scheme used in the global simulations) shows the MWIR and SWIR are most sensitive to the parameterization of the  $C_w$ . The tropical site (Figure 9D) is not sensitive to the change in functional form because soil moisture is high enough to not affect  $C_w$ . Further work is needed to relate leaf moisture to fitting  $C_w$  using tower and leaf-level observations or by integrating airborne data, including radar that can retrieve canopy moisture content.

#### *Global-scale characteristics*

The spectral response functions and their seasonal dynamics from the four sites show that LPJ-PROSAIL captures expected variability across biomes, where phenology, soil moisture, and seasonality are different. At the global scale, LPJ-PROSAIL simulated spectra for each grid cell, 0.5-degrees resolution, at a daily temporal resolution. These spectra can be used with empirical algorithms to derive canopy properties as independent verification or evaluation of the LPJ model or to be used to update model states and assess errors and uncertainties. Additionally, vegetation indices can be derived from the simulation as alternative measures for site-level evaluation or spaceborne observations. Figure 10 illustrates how LPJ-PROSAIL NDVI can be derived for the winter and summer months using  $((850\text{nm}-650\text{nm})/(850\text{nm}+650\text{nm}))$  and its comparison to the MOD13C2 v6.1 NDVI product. In January, snow cover and deciduous phenology lead to low NDVI in high latitudes, with fairly high NDVI in the pan-tropics. The differences between LPJ-PROSAIL and MODIS are most noticeable in the mid-latitudes, where land use and agriculture, not included in LPJ-PROSAIL, are causing differences in observed and simulated vegetation. In summer, the main differences are in the southern hemisphere sub-tropical regions, like the cerrado and miombo areas. A combination of land use, disturbance histories, and parameterization of LPJ PFTs are causing mismatches in phenology and can be areas of future model improvement.

#### *E2E applications*

As imaging spectroscopy advances from targeted airborne campaigns to global spaceborne missions, there is an increasing need for advancing modeling tools to provide E2E support and to take advantage of new observations. Here we describe the coupling of a DGVM model with the PROSAIL canopy radiative transfer model and demonstrate a simulation of global daily spectral responses. While our approach makes assumptions to match the theoretical basis of modeling approaches, the cross-walking of parameters, and functional forms, we show at first order that the spectral features and their changes over time compare well to independent observations from tower observations and from spaceborne

instruments. The coupling also shows how key variables in LPJ, such as  $V_{\text{cmax}}$  and LAI, require development to be more consistent with observations.

The coupling of LPJwsl and PROSAIL has identified area of future research to improve the cross-walking of physiological and structural parameters. Future work will consist of improving the structural representation of vegetation, the physiological parameterization, and the calibration of parameters responses using field observations. We intend to move beyond ‘big-leaf’ representation to multi-layer canopy scheme (i.e., Braghieri et al., 2021), and implement an interactive nitrogen scheme where  $V_{\text{cmax}}$  can be better partitioned to inform PROSPECT-5b (Zhang et al., 2017). Functional forms of LPJ-PROSAIL parameters will be derived using tower (i.e., SpecNet) or airborne (i.e., National Ecological Observation Network, NEON) time series. Assumptions for the 4SAIL parameterization will be explored by evaluating changes in assumptions for leaf angle distributions (*lidf*) by PFT (planophile, erectophile, plagiophile, extremophile, and uniform). Simulations will be set up to use land use, improving some of the PFT representation in heavily managed regions. The developments also enable dynamic-trait modeling to be further explored, moving away from fixed-trait modeling that many land surface models have relied on for the past two decades (Verheijen et al., 2013, Trugman et al., 2022). In addition, model experiments can be carried out to understand spectral responses to climate trends, climate extremes, natural disturbances such as fire, and vegetation stress to water shortages.

The remote intercomparison experiment underscores the need for continued improvement in instrument calibration and atmospheric correction. Differences between remote and in-situ reflectances were far larger than the discrepancy between the model and in situ data. This suggests that, even if models were perfect, the remote data might not be sufficient to accurately estimate LPJ-PROSAIL parameters. Previous studies of trait measurements often rely on limited airborne campaigns with careful, manual attention to instrument calibration and atmospheric correction. Operational trait estimation on global scales will require similarly high-fidelity estimates of surface reflectance to be produced automatically. Reconciling model predictions with remote data will require continual progress to improve atmospheric correction uncertainties.

LPJ-PROSAIL creates opportunities for both informing mission design and to also enable the global Earth system modeling community to be able to take advantage of upcoming missions (Angel and McCabe 2022). The LPJ-PROSAIL model will be used for mission support via OSSE experiments that will help quantify mission performance and improvements to the carbon and hydrologic cycles, core science focal areas for NASA’s SBG mission.

### **Acknowledgments**

We acknowledge support from the NASA Surface Biology and Geology Designated Observable architecture study. Part of the research described in this paper was carried out at the Jet Propulsion Laboratory, California Institute

of Technology, under contract with the National Aeronautics and Space Administration. Government sponsorship acknowledged. This material is also based upon work supported by the National Science Foundation Graduate Research Fellowship under Grant No. DGE-1650604 and DGE-2034835. Any opinion, findings, and conclusions or recommendations expressed in this material are those of the authors(s) and do not necessarily reflect the views of the National Science Foundation. We thank Teledyne Brown Engineering (TBE) and the German Aerospace Center (DLR) for providing the DESIS images. We acknowledge the PRISMA Products, © of the Italian Space Agency (ASI), delivered under an ASI License to use. The code is available on Github, [https://github.com/benpoulter/LPJ-wsl\\_v2.0](https://github.com/benpoulter/LPJ-wsl_v2.0).

## References

- Alonso, K., Bachmann, M., Burch, K., Carmona, E., Cerra, D., de los Reyes, R., et al. (2019). Data Products, Quality and Validation of the DLR Earth Sensing Imaging Spectrometer (DESI). *Sensors*, 19(20), 4471. <https://doi.org/10.3390/s19204471>
- Angel, Y., & McCabe, M. F. (2022). Machine Learning Strategies for the Retrieval of Leaf-Chlorophyll Dynamics: Model Choice, Sequential Versus Retraining Learning, and Hyperspectral Predictors. *Frontiers in Plant Science*, 13. Retrieved from <https://www.frontiersin.org/article/10.3389/fpls.2022.722442>
- Antonarakis, A. S., Bogan, S. A., Goulden, M. L., & Moorcroft, P. R. (2022). Impacts of the 2012–2015 Californian drought on carbon, water and energy fluxes in the Californian Sierras: Results from an imaging spectrometry-constrained terrestrial biosphere model. *Global Change Biology*, 28(5), 1823–1852. <https://doi.org/10.1111/gcb.15995>
- Badgley, G., Anderegg, L. D. L., Berry, J. A., & Field, C. B. (2019). Terrestrial gross primary production: Using NIR<sub>v</sub> to scale from site to globe. *Global Change Biology*, 25(11), 3731–3740. <https://doi.org/10.1111/gcb.14729>
- Braghiere, R. K., Wang, Y., Doughty, R., Sousa, D., Magney, T., Widlowski, J.-L., et al. (2021). Accounting for canopy structure improves hyperspectral radiative transfer and sun-induced chlorophyll fluorescence representations in a new generation Earth System model. *Remote Sensing of Environment*, 261, 112497. <https://doi.org/10.1016/j.rse.2021.112497>
- Calle, L., & Poulter, B. (2021). Ecosystem age-class dynamics and distribution in the LPJ-wsl v2.0 global ecosystem model. *Geoscientific Model Development*, 14(5), 2575–2601. <https://doi.org/10.5194/gmd-14-2575-2021>
- Campbell, A. D., Fatoyinbo, T., Charles, S. P., Bourgeau-Chavez, L. L., Goes, J., Gomes, H., et al. (2022). A review of carbon monitoring in wet carbon systems using remote sensing. *Environmental Research Letters*, 17(2), 025009. <https://doi.org/10.1088/1748-9326/ac4d4d>
- Campbell, M. J., Dennison, P. E., Kerr, K. L., Brewer, S. C., & An-

- deregg, W. R. L. (2021). Scaled biomass estimation in woodland ecosystems: Testing the individual and combined capacities of satellite multi-spectral and lidar data. *Remote Sensing of Environment*, 262, 112511. <https://doi.org/10.1016/j.rse.2021.112511>
- Campbell, P., Huemmrich, K., Middleton, E., Ward, L., Julitta, T., Daughtry, C., et al. (2019). Diurnal and Seasonal Variations in Chlorophyll Fluorescence Associated with Photosynthesis at Leaf and Canopy Scales. *Remote Sensing*, 11(5), 488. <https://doi.org/10.3390/rs11050488>
- Campbell, P. E. K., Huemmrich, K. F., Middleton, E. M., Alfieri, J., van der Tol, C., & Neigh, C. S. R. (2022). Using Desis and EO-1 Hyperion reflectance time series for the assessment of vegetation traits and gross primary production (GPP). In *The International Archives of the Photogrammetry, Remote Sensing and Spatial Information Sciences* (Vol. XLVI-1-W1-2021, pp. 1–8). Copernicus GmbH. <https://doi.org/10.5194/isprs-archives-XLVI-1-W1-2021-1-2022>
- Cawse-Nicholson, K., Raiho, A., Thompson, D. R., Hulley, G., Miller, C. E., Miner, K., et al. (2022, March 23). Intrinsic Dimensionality as a Metric for the Impact of Mission Design Parameters [preprint]. <https://doi.org/10.1002/essoar.10510874.1>
- Chlus, A., & Townsend, P. A. (2022). Characterizing seasonal variation in foliar biochemistry with airborne imaging spectroscopy. *Remote Sensing of Environment*, 275, 113023. <https://doi.org/10.1016/j.rse.2022.113023>
- Cogliati, S., Sarti, F., Chiarantini, L., Cosi, M., Lorusso, R., Lopinto, E., et al. (2021). The PRISMA imaging spectroscopy mission: overview and first performance analysis. *Remote Sensing of Environment*, 262, 112499. <https://doi.org/10.1016/j.rse.2021.112499>
- Connelly, D. S., Thompson, D. R., Mahowald, N. M., Li, L., Carmon, N., Okin, G. S., & Green, R. O. (2021). The EMIT mission information yield for mineral dust radiative forcing. *Remote Sensing of Environment*, 258, 112380. <https://doi.org/10.1016/j.rse.2021.112380>
- Croft, H., Chen, J. M., Luo, X., Bartlett, P., Chen, B., & Staebler, R. M. (2017). Leaf chlorophyll content as a proxy for leaf photosynthetic capacity. *Global Change Biology*, 23(9), 3513–3524. <https://doi.org/10.1111/gcb.13599>
- Danner, M., Berger, K., Wocher, M., Mauser, W., & Hank, T. (2019). Fitted PROSAIL Parameterization of Leaf Inclinations, Water Content and Brown Pigment Content for Winter Wheat and Maize Canopies. *Remote Sensing*, 11(10), 1150. <https://doi.org/10.3390/rs11101150>
- Fan, Y., Li, W., Chen, N., Ahn, J.-H., Park, Y.-J., Kratzer, S., et al. (2021). OC-SMART: A machine learning based data analysis platform for satellite ocean color sensors. *Remote Sensing of Environment*, 253, 112236. <https://doi.org/10.1016/j.rse.2020.112236>

- Farquhar, G. D., von Caemmerer, S., & Berry, J. A. (1980). A biochemical model of photosynthetic CO<sub>2</sub> assimilation in leaves of C<sub>3</sub> species. *Planta*, 149(1), 78–90. <https://doi.org/10.1007/BF00386231>
- Feret, J.-B., François, C., Asner, G. P., Gitelson, A. A., Martin, R. E., Bidel, L. P. R., et al. (2008). PROSPECT-4 and 5: Advances in the leaf optical properties model separating photosynthetic pigments. *Remote Sensing of Environment*, 112(6), 3030–3043. <https://doi.org/10.1016/j.rse.2008.02.012>
- Fisher, R. A., Koven, C. D., Anderegg, W. R. L., Christoffersen, B. O., Dietze, M. C., Farnior, C. E., et al. (2018). Vegetation demographics in Earth System Models: A review of progress and priorities. *Global Change Biology*, 24(1), 35–54. <https://doi.org/10.1111/gcb.13910>
- Folkman, M, J. Pearlman, L. Liao, and P. Jarecke. (2001). EO-1/Hyperion hyperspectral imager design, development, characterization, and calibration, in *Proc. SPIE Hyperspectral Remote Sens. Land Atmos.*, vol. 4151, pp. 40–51.
- Gamon, J. A., Somers, B., Malenovský, Z., Middleton, E. M., Rascher, U., & Schaepman, M. E. (2019). Assessing Vegetation Function with Imaging Spectroscopy. *Surveys in Geophysics*, 40(3), 489–513. <https://doi.org/10.1007/s10712-019-09511-5>
- Gao, B.-C., Heidebrecht, K. B., & Goetz, A. F. H. (1993). Derivation of scaled surface reflectances from AVIRIS data. *Remote Sensing of Environment*, 44(2–3), 165–178. [https://doi.org/10.1016/0034-4257\(93\)90014-O](https://doi.org/10.1016/0034-4257(93)90014-O)
- Gastellu-Etchegorry, J.-P., Yin, T., Lauret, N., Cajgfinger, T., Gregoire, T., Grau, E., et al. (2015). Discrete Anisotropic Radiative Transfer (DART 5) for Modeling Airborne and Satellite Spectroradiometer and LIDAR Acquisitions of Natural and Urban Landscapes. *Remote Sensing*, 7(2), 1667–1701. <https://doi.org/10.3390/rs70201667>
- Gates, D. M., Keegan, H. J., Schleter, J. C., & Weidner, V. R. (1965). Spectral Properties of Plants. *Applied Optics*, 4(1), 11–20. <https://doi.org/10.1364/AO.4.000011>
- Goodenough, A. A., & Brown, S. D. (2012). DIRSIG 5: core design and implementation. In *Algorithms and Technologies for Multispectral, Hyperspectral, and Ultraspectral Imagery XVIII* (Vol. 8390, pp. 124–132). SPIE. <https://doi.org/10.1117/12.919321>
- Gregg, W. W., & Rousseaux, C. S. (2017). Simulating PACE Global Ocean Radiances. *Frontiers in Marine Science*, 4. <https://doi.org/10.3389/fmars.2017.00060>
- Grossmann, K., Frankenberg, C., Magney, T. S., Hurlock, S. C., Seibt, U., & Stutz, J. (2018). PhotoSpec: A new instrument to measure spatially distributed red and far-red Solar-Induced Chlorophyll Fluorescence. *Remote Sensing of Environment*, 216, 311–327. <https://doi.org/10.1016/j.rse.2018.07.002>
- Harris, I., Osborn, T. J., Jones, P., & Lister, D. (2020). Version 4 of the CRU TS monthly high-resolution gridded multivariate climate dataset. *Scientific Data*, 7(1), 109. <https://doi.org/10.1038/s41597-020-0453-3>

- Haxeltine, A., & Prentice, I. C. (1996). BIOME3: An equilibrium terrestrial biosphere model based on ecophysiological constraints, resource availability, and competition among plant functional types. *Global Biogeochemical Cycles*, 10(4), 693–709. <https://doi.org/10.1029/96GB02344>
- Huete, A., Didan, K., Miura, T., Rodriguez, E. P., Gao, X., & Ferreira, L. G. (2002). Overview of the radiometric and biophysical performance of the MODIS vegetation indices. *Remote Sensing of Environment*, 83(1–2), 195–213. [https://doi.org/10.1016/S0034-4257\(02\)00096-2](https://doi.org/10.1016/S0034-4257(02)00096-2)
- Jacquemoud, S., & Ustin, S. (2019). *Leaf Optical Properties*. Cambridge University Press.
- Jacquemoud, S., Verhoef, W., Baret, F., Bacour, C., Zarco-Tejada, P. J., Asner, G. P., et al. (2009). PROSPECT+SAIL models: A review of use for vegetation characterization. *Remote Sensing of Environment*, 113, S56–S66. <https://doi.org/10.1016/j.rse.2008.01.026>
- Julitta, T., Burkart, A., Rossini, M., Schickling, A., Colombo, R., Rascher, U., et al. (2017). FloX: A System for Automatic Long-Term Measurements of Top of Canopy Sun Induced Chlorophyll Fluorescence. In *FLEX 2017 Workshop, ESA-ESRIN. ESA: FLEX 2017*. Retrieved from <https://www.jb-hyperspectral.com/products/flox/>
- Kriegler, F. J., Malila, W. A., Nalepka, R. F., & Richardson, W. (1969). Preprocessing transformations and their effects on multispectral recognition. *Remote Sensing of Environment*, VI(97).
- Krutz, D., Müller, R., Knodt, U., Günther, B., Walter, I., Sebastian, I., et al. (2019). The Instrument Design of the DLR Earth Sensing Imaging Spectrometer (DESI). *Sensors*, 19(7), 1622. <https://doi.org/10.3390/s19071622>
- Kuusinen, N., Hovi, A., & Rautiainen, M. (2021). Contribution of woody elements to tree level reflectance in boreal forests. *Silva Fennica*, 55(5). <https://doi.org/10.14214/sf.10600>
- Loizzo, R., Guarini, R., Longo, F., Scopa, T., Formaro, R., Facchinetti, C., & Varacalli, G. (2018). Prisma: The Italian Hyperspectral Mission. In *IGARSS 2018 - 2018 IEEE International Geoscience and Remote Sensing Symposium* (pp. 175–178). Valencia: IEEE. <https://doi.org/10.1109/IGARSS.2018.8518512>
- Meerdink, S. K., Hook, S. J., Roberts, D. A., & Abbott, E. A. (2019). The ECOSTRESS spectral library version 1.0. *Remote Sensing of Environment*, 230, 111196. <https://doi.org/10.1016/j.rse.2019.05.015>
- Middleton, E. M., Campbell, P. K. E., Ong, L., Landis, D. R., Zhang, Q., Neigh, C. S., et al. (2017). Hyperion: The first global orbital spectrometer, earth observing-1 (EO-1) satellite (2000–2017). In *2017 IEEE International Geoscience and Remote Sensing Symposium (IGARSS)* (pp. 3039–3042). Fort Worth, TX: IEEE. <https://doi.org/10.1109/IGARSS.2017.8127639>

- Nieke, J., & Rast, M. (2018). Towards the Copernicus Hyperspectral Imaging Mission For The Environment (CHIME). In IGARSS 2018 - 2018 IEEE International Geoscience and Remote Sensing Symposium (pp. 157–159). <https://doi.org/10.1109/IGARSS.2018.8518384>
- Norton, A. J., Rayner, P. J., Koffi, E. N., Scholze, M., Silver, J. D., & Wang, Y.-P. (2019). Estimating global gross primary productivity using chlorophyll fluorescence and a data assimilation system with the BETHY-SCOPE model. *Biogeosciences*, 16(15), 3069–3093. <https://doi.org/10.5194/bg-16-3069-2019>
- Pierrat, Z., Nehemy, M. F., Roy, A., Magney, T., Parazoo, N. C., Laroque, C., et al. (2021). Tower-Based Remote Sensing Reveals Mechanisms Behind a Two-phased Spring Transition in a Mixed-Species Boreal Forest. *Journal of Geophysical Research: Biogeosciences*, 126(5). <https://doi.org/10.1029/2020JG006191>
- Pierrat, Z., Magney, T., Parazoo, N. C., Grossmann, K., Bowling, D. R., Seibt, U., et al. (2022). Diurnal and Seasonal Dynamics of Solar-Induced Chlorophyll Fluorescence, Vegetation Indices, and Gross Primary Productivity in the Boreal Forest. *Journal of Geophysical Research: Biogeosciences*, 127(2). <https://doi.org/10.1029/2021JG006588>
- Raiho, A., Cawse-Nicholson, K., Chlus, A., Dozier, J., Gierach, M. M., Miner, K., et al. (2022, March 29). Exploring mission design for imaging spectroscopy retrievals for land and aquatic ecosystems [preprint]. <https://doi.org/10.1002/essoar.10510949.1>
- Rast, M., & Painter, T. H. (2019). Earth Observation Imaging Spectroscopy for Terrestrial Systems: An Overview of Its History, Techniques, and Applications of Its Missions. *Surveys in Geophysics*, 40(3), 303–331. <https://doi.org/10.1007/s10712-019-09517-z>
- Roberts, D. A., Ustin, S. L., Ogunjemiyo, S., Greenberg, J., Dobrowski, S. Z., Chen, J., & Hinckley, T. M. (2004). Spectral and Structural Measures of Northwest Forest Vegetation at Leaf to Landscape Scales. *Ecosystems*, 7(5). <https://doi.org/10.1007/s10021-004-0144-5>
- Schaepman-Strub, G., Schaepman, M. E., Painter, T. H., Dangel, S., & Martonchik, J. V. (2006). Reflectance quantities in optical remote sensing—definitions and case studies. *Remote Sensing of Environment*, 103(1), 27–42. <https://doi.org/10.1016/j.rse.2006.03.002>
- Schimmel, D and B Poulter. 2022. The Earth in Living Color. IEEE Aerospace Proceedings.
- Schott, J. R., Brown, S. D., Raqueño, R. V., Gross, H. N., & Robinson, G. (1999). An Advanced Synthetic Image Generation Model and its Application to Multi/Hyperspectral Algorithm Development. *Canadian Journal of Remote Sensing*, 25(2), 99–111. <https://doi.org/10.1080/07038992.1999.10874709>

- Sellers, P. J. (1985). Canopy reflectance, photosynthesis and transpiration. *International Journal of Remote Sensing*, 6(8), 1335–1372. <https://doi.org/10.1080/01431168508948283>
- Shiklomanov, A. N., Bond-Lamberty, B., Atkins, J. W., & Gough, C. M. (2020). Structure and parameter uncertainty in centennial projections of forest community structure and carbon cycling. *Global Change Biology*, 26(11), 6080–6096. <https://doi.org/10.1111/gcb.15164>
- Shiklomanov, A. N., Dietze, M. C., Fer, I., Viskari, T., & Serbin, S. P. (2021). Cutting out the middleman: calibrating and validating a dynamic vegetation model (ED2-PROSPECT5) using remotely sensed surface reflectance. *Geoscientific Model Development*, 14(5), 2603–2633.
- Shull, C. A. (1929). A Spectrophotometric Study of Reflection of Light from Leaf Surfaces. *Botanical Gazette*, 87(5), 583–607. <https://doi.org/10.1086/333965>
- Sitch, S., Smith, B., Prentice, I. C., Arneth, A., Bondeau, A., Cramer, W., et al. (2003). Evaluation of ecosystem dynamics, plant geography and terrestrial carbon cycling in the LPJ dynamic global vegetation model: LPJ DYNAMIC GLOBAL VEGETATION MODEL. *Global Change Biology*, 9(2), 161–185. <https://doi.org/10.1046/j.1365-2486.2003.00569.x>
- Stamnes, K., Tsay, S.-C., Wiscombe, W., & Jayaweera, K. (1988). Numerically stable algorithm for discrete-ordinate-method radiative transfer in multiple scattering and emitting layered media. *Applied Optics*, 27(12), 2502. <https://doi.org/10.1364/AO.27.002502>
- Stavros, E. N., Chrono, J., Cawse-Nicholson, K., Freeman, A., Glenn, N. F., Guild, L., et al. (n.d.). Designing an Observing System to Study the Surface Biology and Geology of the Earth in the 2020s. *Journal of Geophysical Resources: Biogeosciences*. <https://doi.org/10.1029/2021JG006471>
- Thompson, D. R., Gao, B.-C., Green, R. O., Roberts, D. A., Dennison, P. E., & Lundeen, S. R. (2015). Atmospheric correction for global mapping spectroscopy: ATREM advances for the HypIRI preparatory campaign. *Remote Sensing of Environment*, 167, 64–77. <https://doi.org/10.1016/j.rse.2015.02.010>
- Thompson, D. R., Natraj, V., Green, R. O., Helmlinger, M. C., Gao, B.-C., & Eastwood, M. L. (2018). Optimal estimation for imaging spectrometer atmospheric correction. *Remote Sensing of Environment*, 216, 355–373. <https://doi.org/10.1016/j.rse.2018.07.003>
- Trugman, A. T. (2022). Integrating plant physiology and community ecology across scales through trait-based models to predict drought mortality. *New Phytologist*, 234(1), 21–27. <https://doi.org/10.1111/nph.17821>
- Tucker, C. J., & Sellers, P. J. (1986). Satellite remote sensing of primary production. *International Journal of Remote Sensing*, 7(11), 1395–1416. <https://doi.org/10.1080/01431168608948944>

Tucker, Compton J. (1979). Red and photographic infrared linear combinations for monitoring vegetation. *Remote Sensing of Environment*, 8(2), 127–150. [https://doi.org/10.1016/0034-4257\(79\)90013-0](https://doi.org/10.1016/0034-4257(79)90013-0)

Verheijen, L. M., Brovkin, V., Aerts, R., Bönisch, G., Cornelissen, J. H. C., Kattge, J., et al. (2013). Impacts of trait variation through observed trait–climate relationships on performance of an Earth system model: a conceptual analysis. *Biogeosciences*, 10(8), 5497–5515. <https://doi.org/10.5194/bg-10-5497-2013>

Verhoef, W., & Bach, H. (2007). Coupled soil–leaf–canopy and atmosphere radiative transfer modeling to simulate hyperspectral multi-angular surface reflectance and TOA radiance data. *Remote Sensing of Environment*, 109(2), 166–182. <https://doi.org/10.1016/j.rse.2006.12.013>

Verrelst, J., De Grave, C., Amin, E., Reyes, P., Morata, M., Portales, E., et al. (2021). Prototyping Vegetation Traits Models in the Context of the Hyperspectral Chime Mission Preparation. In *2021 IEEE International Geoscience and Remote Sensing Symposium IGARSS* (pp. 7678–7681). <https://doi.org/10.1109/IGARSS47720.2021.9554407>

Verrelst, Jochem, Rivera-Caicedo, J. P., Reyes-Muñoz, P., Morata, M., Amin, E., Tagliabue, G., et al. (2021). Mapping landscape canopy nitrogen content from space using PRISMA data. *ISPRS Journal of Photogrammetry and Remote Sensing*, 178, 382–395. <https://doi.org/10.1016/j.isprsjprs.2021.06.017>

Wold, S, M Sjostrom, and L Eriksson. (2001). PLS-regression: a basic tool of chemometrics. *Chemometrics and Intelligent Laboratory Systems*, 58:109-130.

Yuan, H., Dai, Y., Dickinson, R. E., Pinty, B., Shangguan, W., Zhang, S., et al. (2017). Reexamination and further development of two-stream canopy radiative transfer models for global land modeling: Improvement of two-stream canopy model. *Journal of Advances in Modeling Earth Systems*, 9(1), 113–129. <https://doi.org/10.1002/2016MS000773>

Zhang, Y., Huang, J., Wang, F., Blackburn, G. A., Zhang, H. K., Wang, X., et al. (2017). An extended PROSPECT: Advance in the leaf optical properties model separating total chlorophylls into chlorophyll a and b. *Scientific Reports*, 7(1), 6429. <https://doi.org/10.1038/s41598-017-06694-y>

Figure 1: (A) Locations of the four intensive sites across North and Central America. The sites (B-E) were selected to be representative of temperature, moisture, and phenology gradients and for locations where tower or remote sensing data were accessible. The base map for (A) is the simulated reflectance for June at 550 nm.

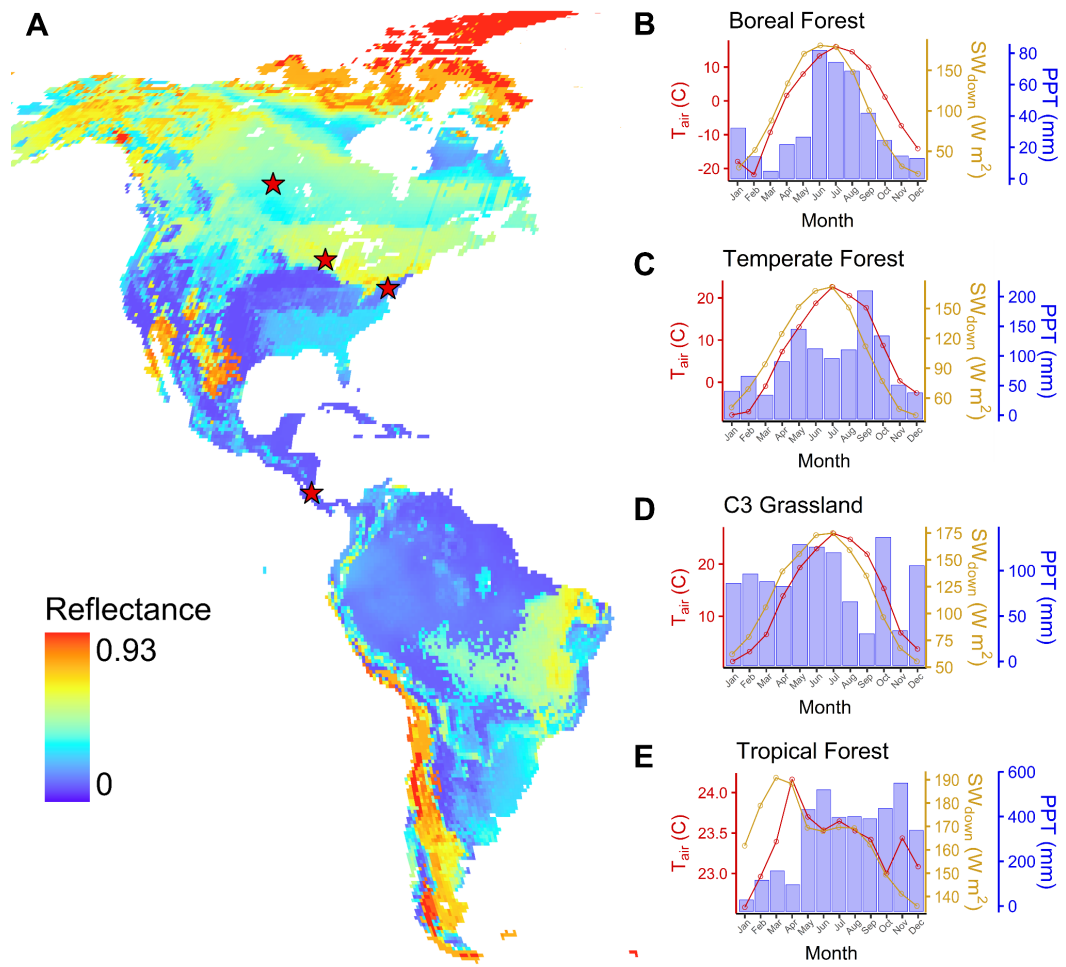


Figure 2: (A) interpretation of VSWIR spectral response and the sensitivity to biochemical and structural constituents (where  $N= 1.2$ ,  $C_w= 0.009$ ,  $C_{ar}= 8$ ,  $C_{ab}= 15$ ,  $C_m= 0.005$ ,  $C_{brown}= 0.01$ ), and (B) functional form selected to estimate variability in leaf water content ( $C_w$ ) as a function of simulated upper layer (0-0.5 m) soil moisture.

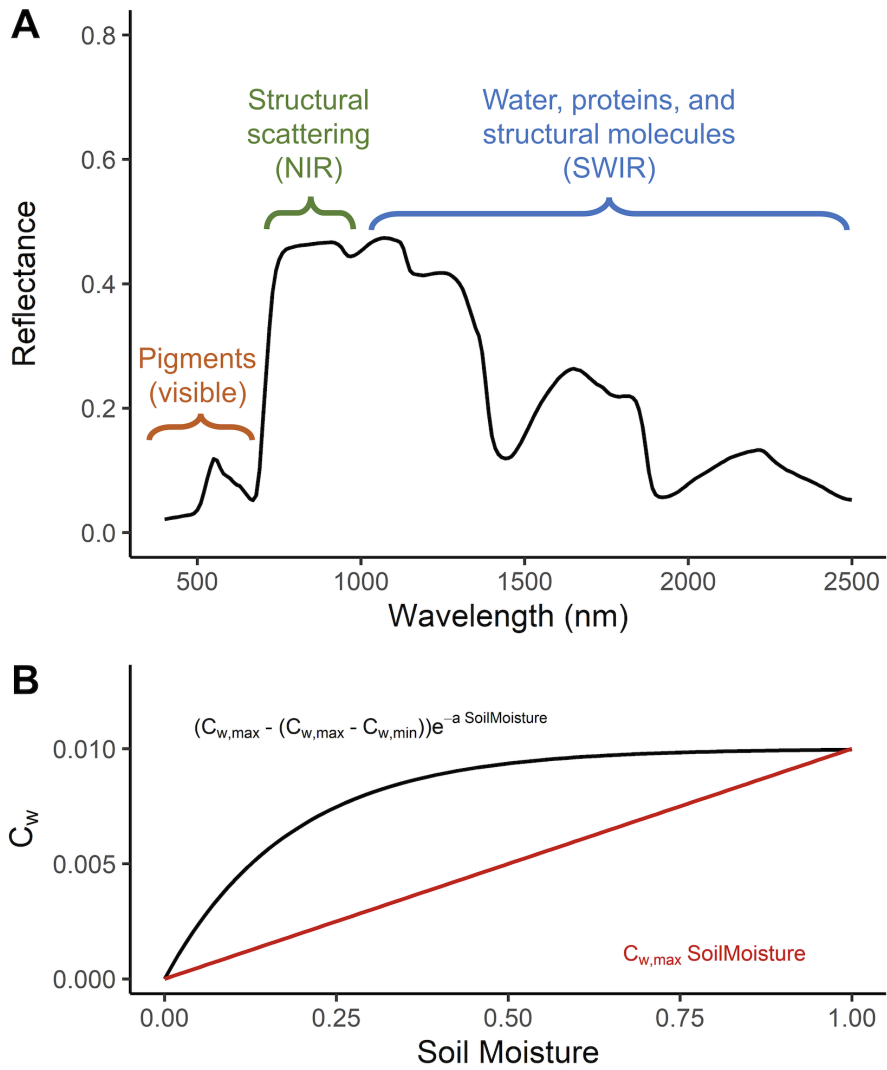


Figure 3: (A) Monthly spectra from Equation 1 for the boreal evergreen forest site for representative year (2020), (B) monthly leaf area index (LAI) for the plant functional types (PFT) location at the site, (C) monthly  $V_{cmax}$  for the same PFTs in (B), (D) monthly snowpack dynamics, and (E) monthly leaf water content weighted by PFT fractional area.

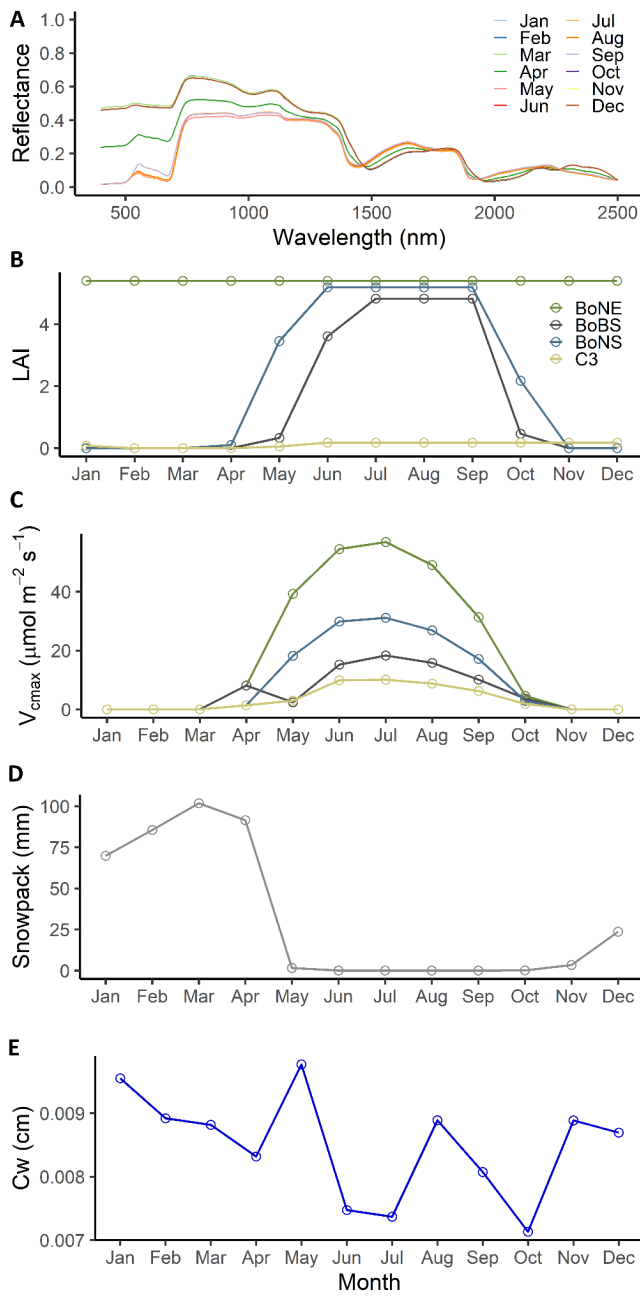


Figure 4: (A) Monthly spectra for the temperate deciduous forest site for representative year (2020), (B) monthly leaf area index (LAI) for the plant functional types (PFT) location at the site, (C) monthly  $V_{cmax}$  for the same PFTs in (B), (D) monthly snowpack dynamics, and (E) monthly leaf water content weighted

by PFT fractional area.

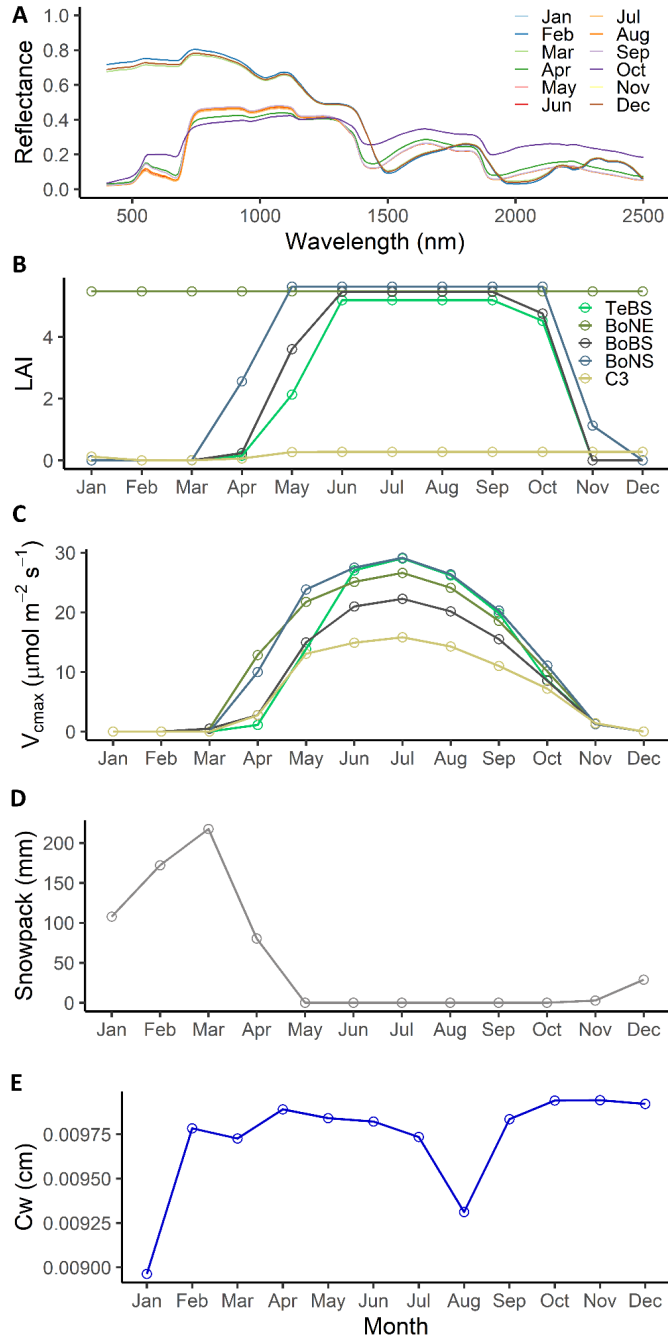


Figure 5: (A) Monthly spectra for the temperate C3 managed grassland site

for representative year (2020), (B) monthly leaf area index (LAI) for the plant functional types (PFT) location at the site, (C) monthly  $V_{cmax}$  for the same PFTs in (B), (D) monthly snowpack dynamics, and (E) monthly leaf water content weighted by PFT fractional area.

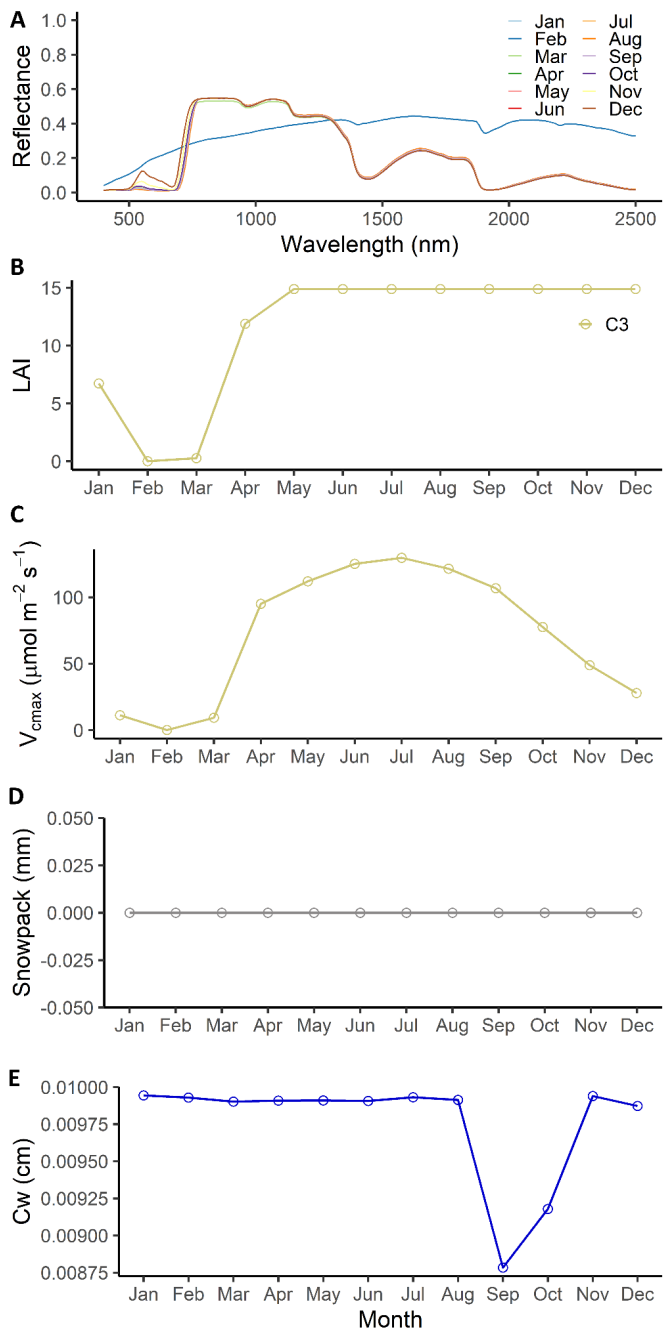


Figure 6: (A) Monthly spectra for the tropical evergreen forest site for representative year (2020), (B) monthly leaf area index (LAI) for the plant functional types (PFT) location at the site, (C) monthly  $V_{cmax}$  for the same PFTs in (B),

(D) monthly snowpack dynamics, and (E) monthly leaf water content weighted by PFT fractional area.

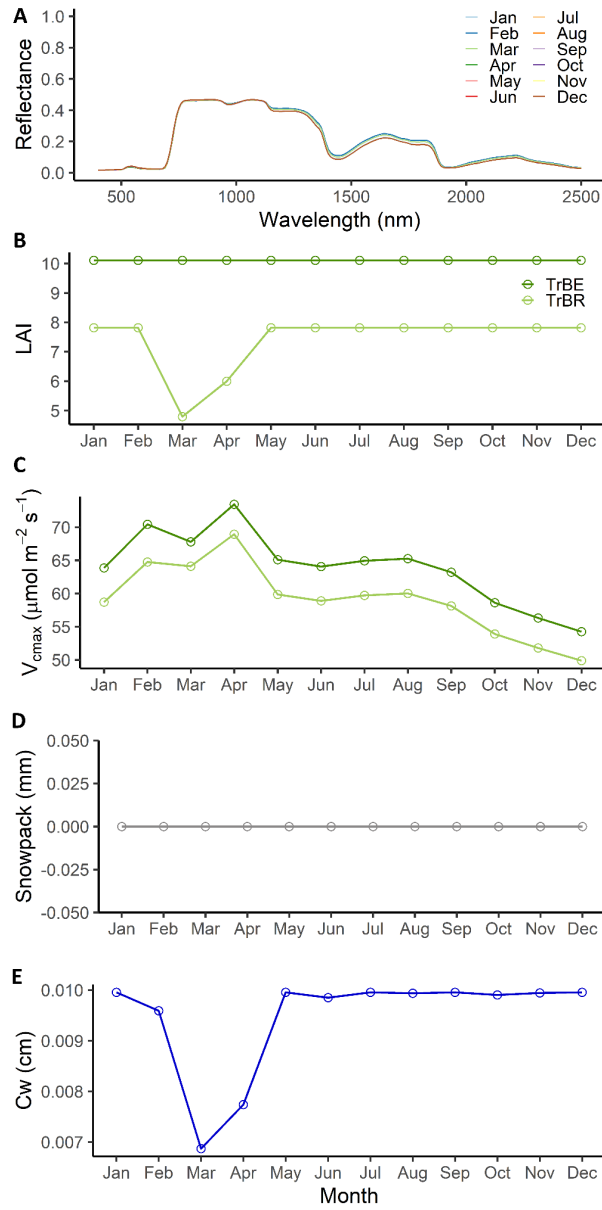


Figure 7: Comparison of August 2020 spectra for the four sites (A-D) and the available in-situ (i.e., PhotSpec) and spaceborne observations (AVIRIS-NG, DESIS, PRISMA).

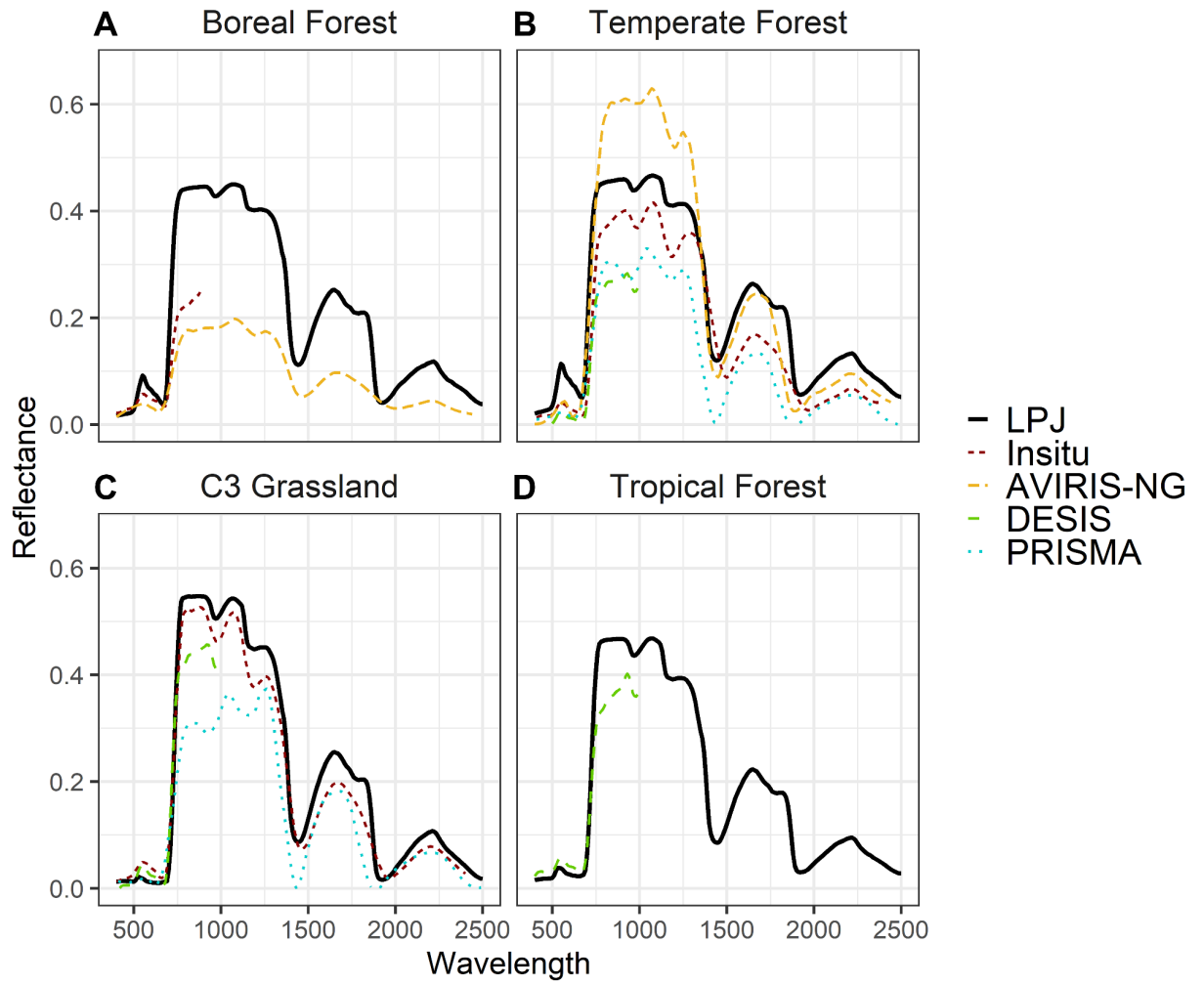


Figure 8: - Hoevmueller plots illustrating the full temporal variation in spectra for each of the four sites (A-D).

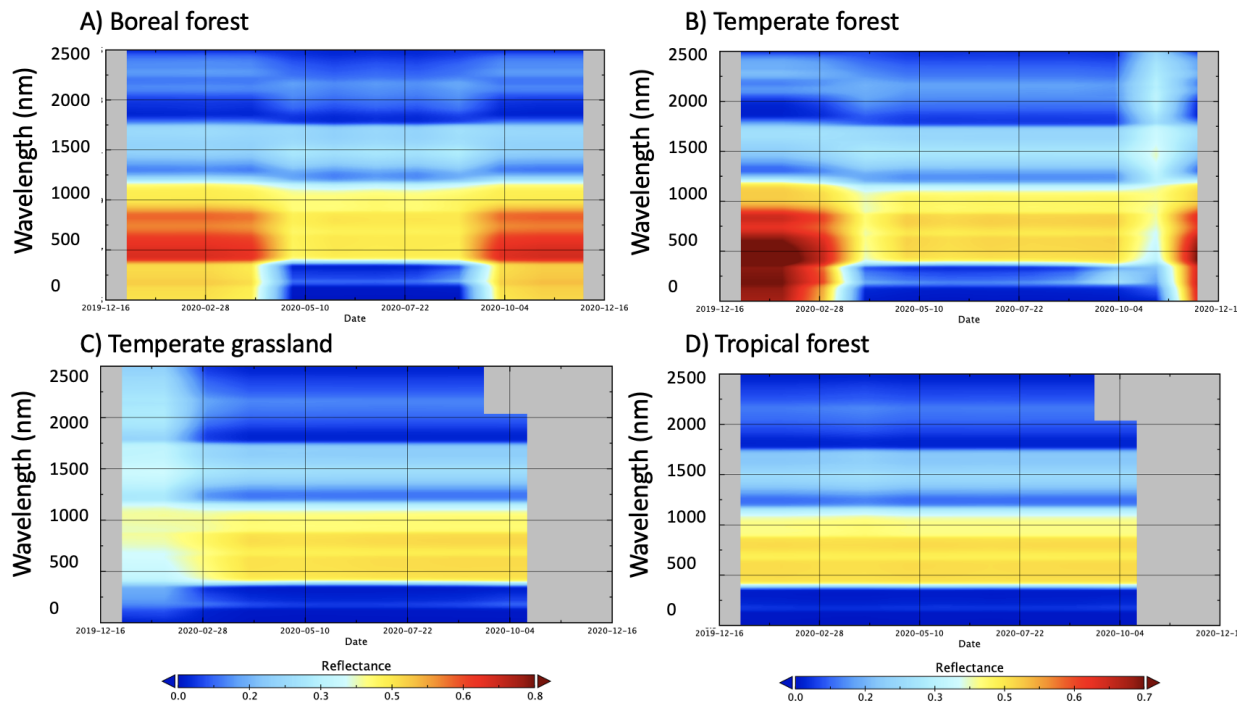


Figure 9: Spectra for two functional forms of leaf water content,  $C_w$ , for month of June (2020), for each of the four sites (A-D).

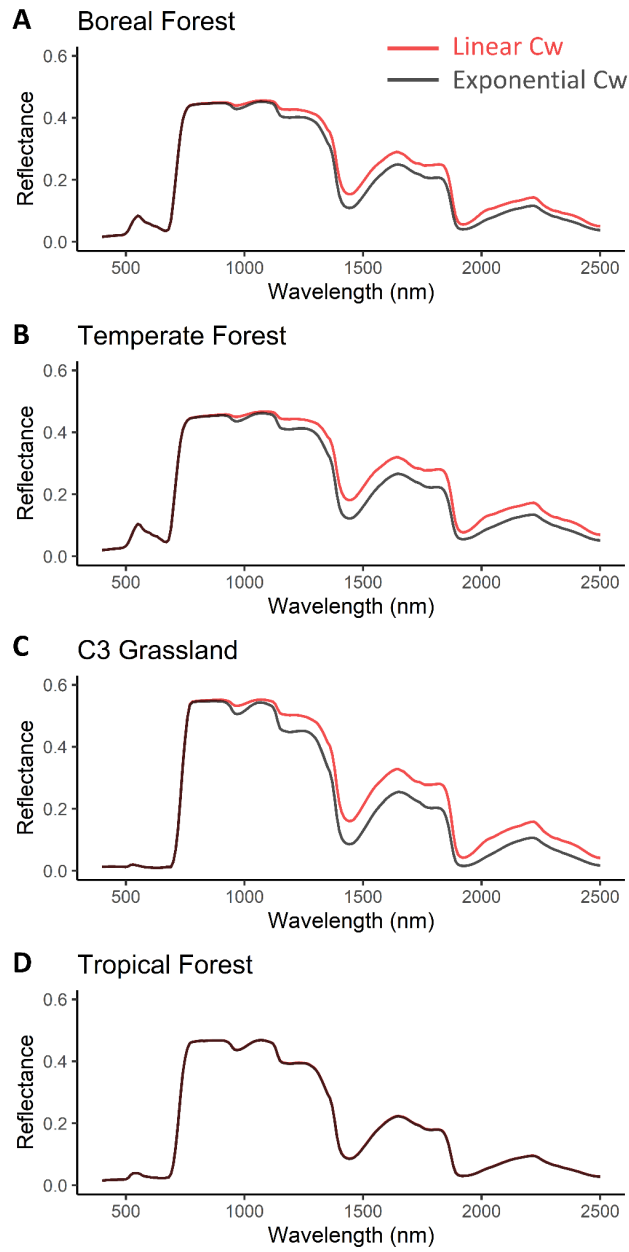


Figure 10: Derived global NDVI  $\left(\frac{850\text{nm}-650\text{nm}}{850\text{nm}+650\text{nm}}\right)$  for 2020 January (A) and for July (B), compared to MODIS (MOD13C2 v6.1) (C-D), and the difference between MODIS and LPJ-PROSAIL (E-F).

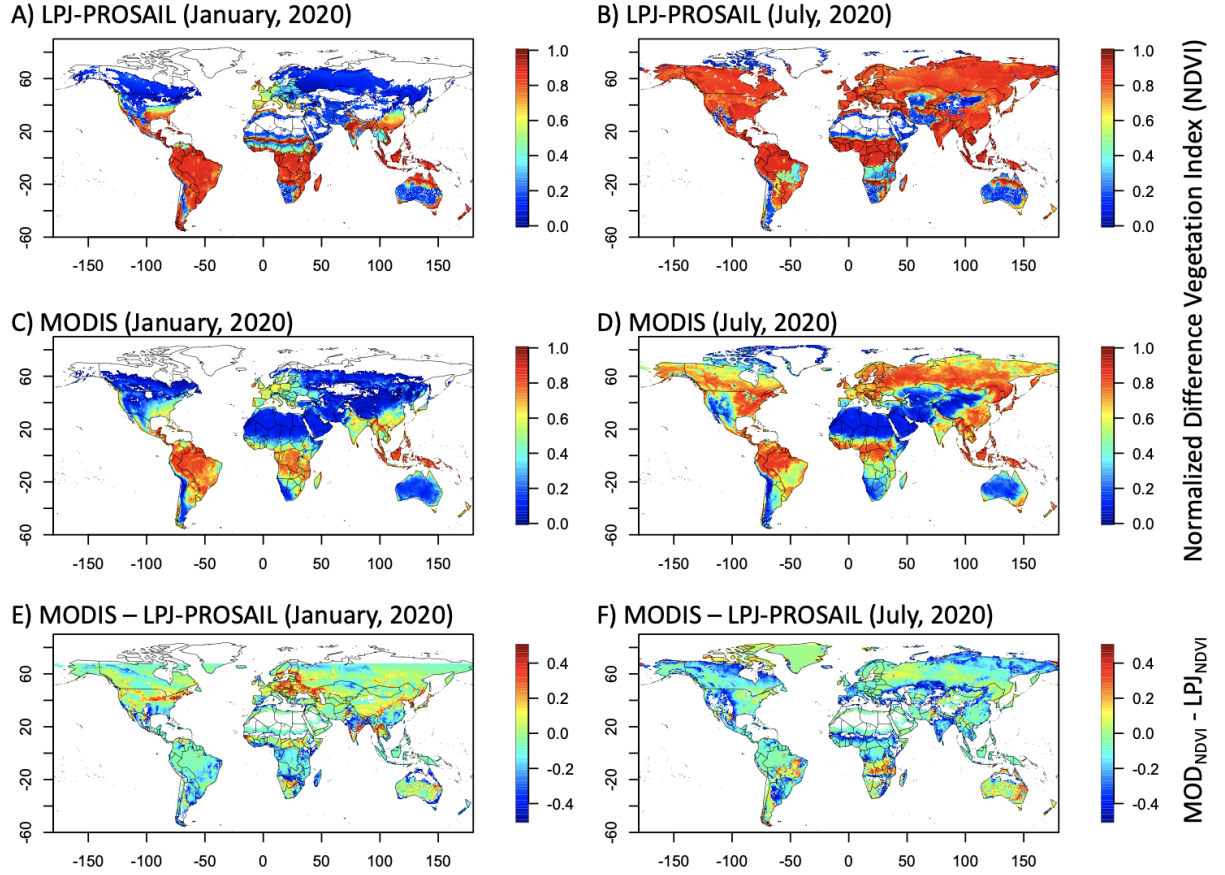
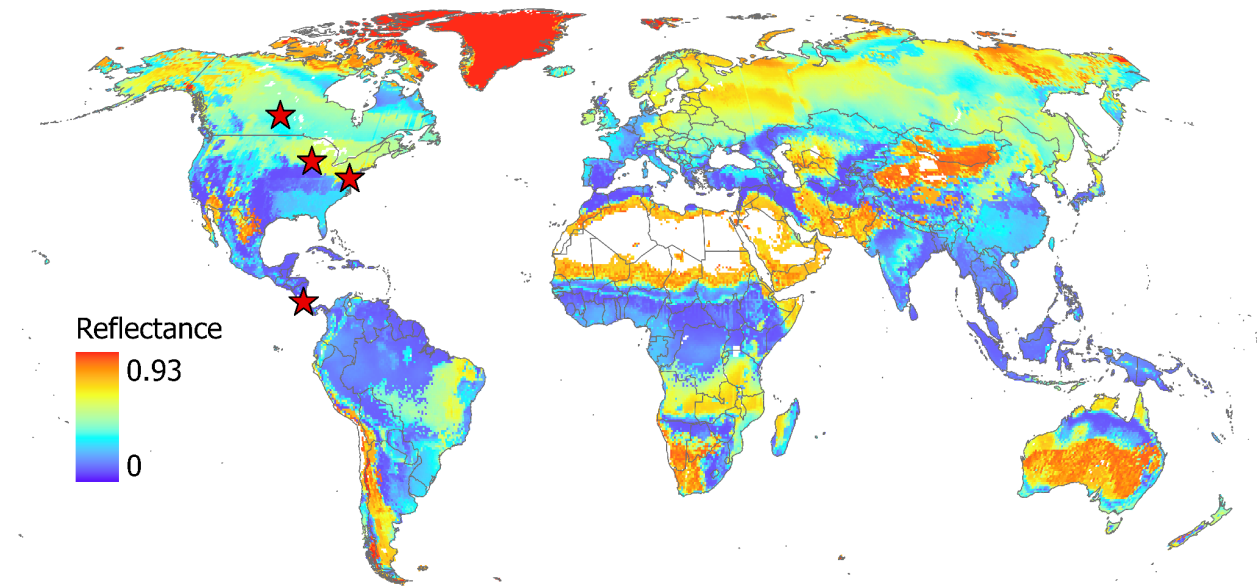


Table 1: Parameters used in initializing the PROSAIL model and how they vary by PFT and time.

| PROSPECT-5b parameter                        |  | Var. name | Unit              | Value            | Variability  | So  |
|--|--|-----------|-------------------|------------------|--------------|-----|
| Leaf structure parameter                     |  | n_layer   | --                | f(SLA)           | PFT, daily   | Jac |
| Chlorophyll a+b conc.                        |  | Cab       | g/cm <sup>2</sup> | f ( Vcmax )      | PFT, daily   | Cr  |
| Carotenoid conc.                             |  | Car       | g/cm <sup>2</sup> | 8.0              | --           | Fer |
| Brown Pigment                                |  | Cbrown    | --                | 0.01             | --           | Fer |
| Equivalent water thickness                   |  | Cw        | cm                | f ( LAI*phen )   | PFT, daily   | see |
| Dry matter content                           |  | Cm        | g/cm <sup>2</sup> | 1/SLA            | PFT, yearly  | n/a |
| 4SAIL parameter                              |  | Var. name | Unit              | Value            | Variability  | So  |
| Leaf Area Index                              |  | LAI       | --                | LAI*phen         | PFT, daily   | Sit |
| Dry/wet soil reflectance                     |  | $p_s$     | --                | f(soil moisture) | Tile, daily  | To  |
| Hotspot parameter                            |  | hspot     | --                | 0.01             | --           |     |
| Ratio of diffuse to total incident radiation |  | SKYL      | --                | 0-1              | Lat,DOY,time |     |
| Solar Zenith Angle                           |  | tts       | deg               | --               | Lat,DOY,time | Pie |
| Sun-Observer Zenith Angle                    |  | tto       | deg               | 0°               | --           | As  |

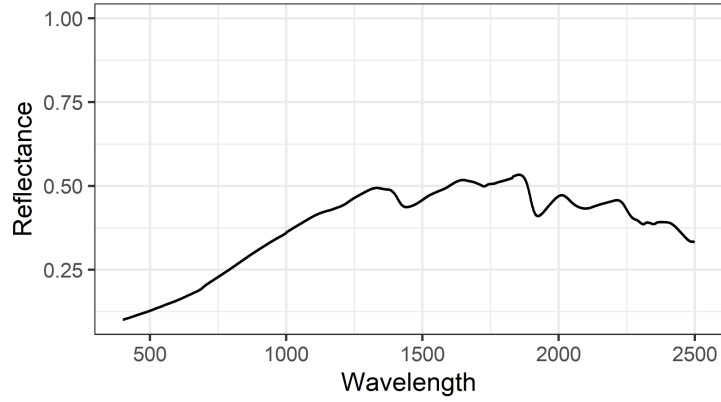
|   |          |     |    |              |     |
|---|----------|-----|----|--------------|-----|
| Relative Azimuth Angle                        | psi      | deg | -- | Lat,DOY,time | Pic |
| Distribution of leaf angles within the canopy | TypeLidf | --  | 1  | --           | Ja  |

Supplementary Figure 1: Global map of 550 nm reflectance for Aug 2019 (same as in Figure 1A, but global) with stars indicating location of the four intensive sites.

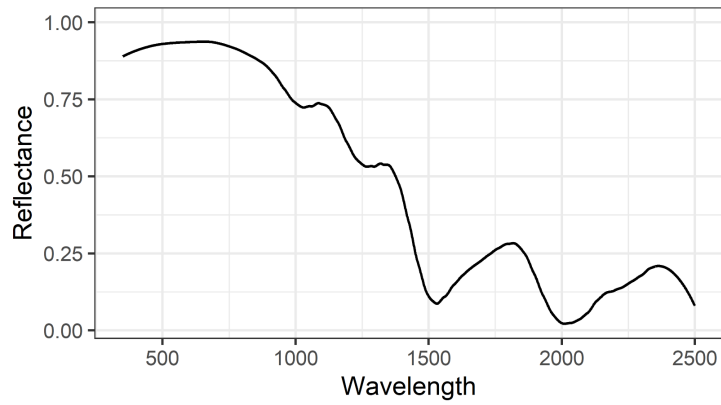


Supplementary Figure 2: Representative spectra used for mixing (A) branch and (B) snow in Equations 10-13.

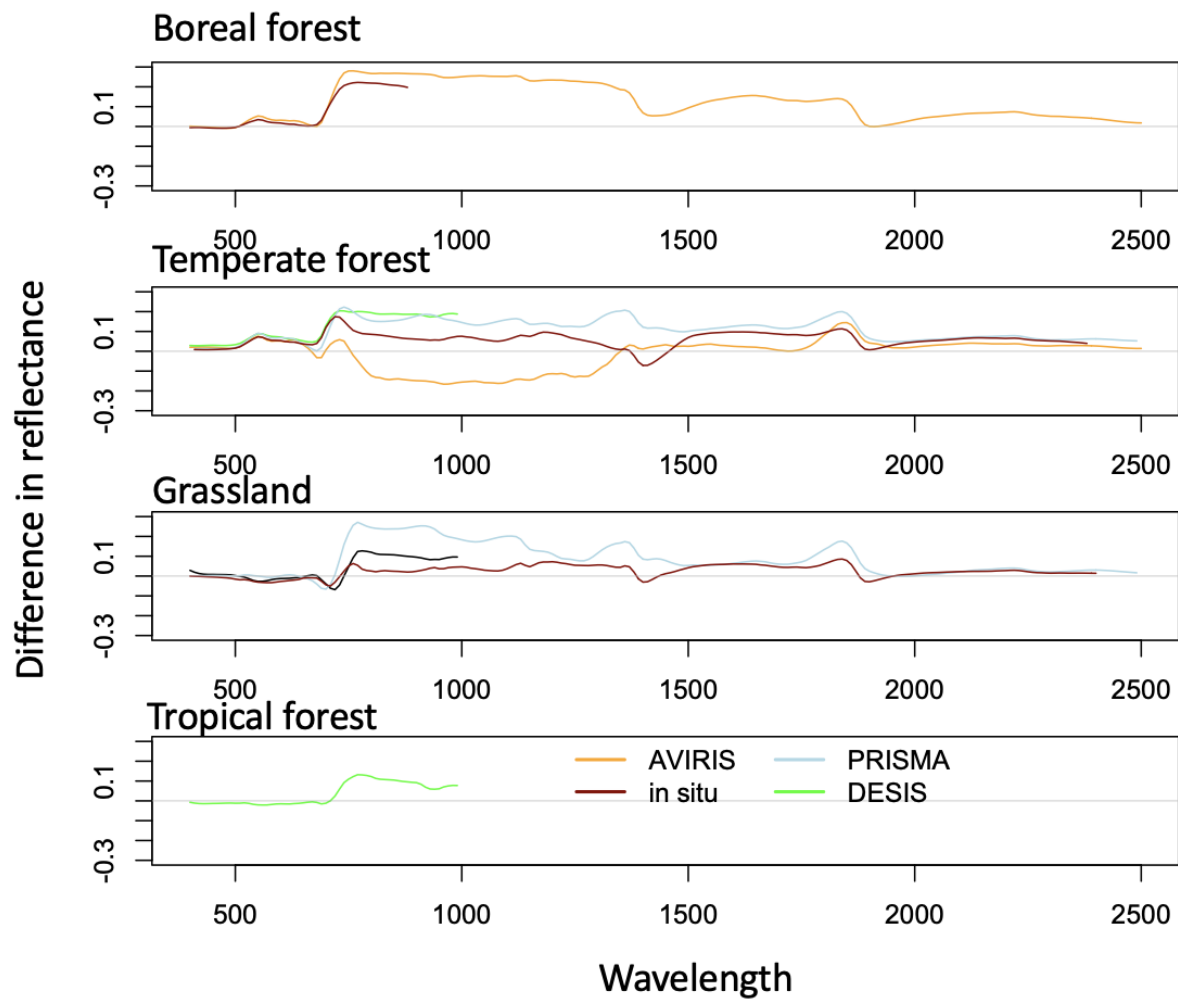
**A** Branch



**B** Snow



Supplementary Figure 3: Difference between (July 2020) spectra for the four sites (A-D) and the available in-situ (i.e., PhotSpec) and spaceborne observations (DESI and PRISMA).



Supplementary Figure 4: Density plot of January 2020 MODIS and LPJ-PROSAIL NDVI. From Figure 10.

